



**HAL**  
open science

## Low-Temperature Hot Corrosion Behavior of DS200 + Hf Nickel-Based Superalloy At 650 °C

Grégoire Dufour, Damien Texier, T. Sanviemvongsak, T. Perez, J. Bonnal, S. Knittel, David Bonina, Michel Vilasi, S. Mathieu

► **To cite this version:**

Grégoire Dufour, Damien Texier, T. Sanviemvongsak, T. Perez, J. Bonnal, et al.. Low-Temperature Hot Corrosion Behavior of DS200 + Hf Nickel-Based Superalloy At 650 °C. High Temperature Corrosion of Materials, 2024, 101, pp.1027-1039. 10.1007/s11085-024-10262-x . hal-04678443

**HAL Id: hal-04678443**

<https://imt-mines-albi.hal.science/hal-04678443v1>

Submitted on 3 Sep 2024

**HAL** is a multi-disciplinary open access archive for the deposit and dissemination of scientific research documents, whether they are published or not. The documents may come from teaching and research institutions in France or abroad, or from public or private research centers.

L'archive ouverte pluridisciplinaire **HAL**, est destinée au dépôt et à la diffusion de documents scientifiques de niveau recherche, publiés ou non, émanant des établissements d'enseignement et de recherche français ou étrangers, des laboratoires publics ou privés.

# Low-Temperature Hot Corrosion Behavior of DS200 + Hf Nickel-Based Superalloy At 650 °C

G. Dufour<sup>1,2,3</sup> · D. Texier<sup>2</sup> · T. Sanviemvongsak<sup>3</sup> · T. Perez<sup>3</sup> · J. Bonnal<sup>4</sup> · S. Knittel<sup>4</sup> · D. Bonina<sup>1</sup> · M. Vilasi<sup>1</sup> · S. Mathieu<sup>1</sup>

## Abstract

The morphologies of Type-II hot corrosion attacks were investigated at 650 °C for the DS200 + Hf nickel-based superalloy. The relationship between corrosion rate and microstructural features, i.e., grain boundaries, carbides, eutectics, dendrites, was considered at different scales and for three environments. Corrosion tests and related characterizations were carried out on a total of forty-five samples, including different sampling strategies, test conditions (air, air + 150 ppm SO<sub>2</sub> and air + 400 ppm SO<sub>2</sub>) and exposure times (24, 50 and 100 h). The amount of SO<sub>2</sub> in the inlet gas was found to be the main factor in the degradation, affecting both the duration of the incubation period and directly the corrosion rate. The proportion of grain boundaries as well as their orientation did not have any influence on the degradation kinetics. On the contrary, MC carbides and  $\gamma + \gamma'$  eutectic pools, i.e., the interdendritic area resulting from the solidification stage, underwent deeper attacks for all gaseous atmospheres. The global mechanism can be explained by the SO<sub>3</sub>-induced hot corrosion mechanism.

**Keywords** Hot corrosion ·  $\gamma/\gamma'$  superalloy · Solidification structure · Grain size · Sulfur trioxide

## Introduction

Initially introduced by Pratt and Whitney in the 1970s, DS200 + Hf is a directionally solidified  $\gamma/\gamma'$  nickel-based superalloy, used for turbine blades on multiple aero engines. Its microstructure is defined by predominantly  $\langle 001 \rangle$  oriented columnar grains with high  $\gamma'$  volume fraction ( $\approx 60\%$ ) [1]. DS200 + Hf has an inhomogeneous microstructure with micrometric carbides (enriched in heavy elements like Hf, Nb, Ti, W) improving grain boundaries strength at high temperature as well as  $\gamma + \gamma'$

eutectic pools, representing up to 0.25 to 3.0 vol.% [2]-[4]. Carbides are found in blocky (rapid cooling area) and in Chinese script (slow cooling area) morphology in intragranular and intergranular locations [4]. They can also be associated with eutectic pools in the interdendritic regions [4]. MC carbides are stable at low temperatures but tend to react with the surrounding matrix  $\gamma$  (M: Cr, W) in the form of secondary carbides ( $M_{23}C_6$ ,  $M_6C$ ) at grain boundaries, from 760 °C to 980 °C [5]-[6]. This decrease in Cr content in the surrounding matrix may possibly weaken the alloy's resistance to oxidation or hot corrosion. The use of nickel-based superalloys on engines in environments combining mixture of salt spray and unburnt combustion gas residues can indeed induce severe degradations at intermediate temperatures.

The exposure to sodium sulfate deposit and air +  $SO_x$  gas mixtures is the most widely used condition for testing the corrosion resistance to Type-II hot corrosion, occurring between 550 °C and 770 °C [7]-[10]. There is general agreement in the literature that the degradation mechanism is characterized by initiation and propagation phases [7, 11]-[14]. Both are assumed to be initiated by the formation of a molten sulfate mixture on the alloy surface, significantly promoting diffusion [15]. The  $Na_2SO_4$ - $NiSO_4$  and  $Na_2SO_4$ - $CoSO_4$  systems exhibit eutectic temperatures as low as 671 °C and 576 °C, resp. [16]-[17]. The formation of these molten salts requires a minimum  $SO_3$  partial pressure which is a function of the temperature: 12 ppm for  $Na_2SO_4$ - $CoSO_4$  at 650 °C [17]. The molten sulfate mixture can then lead to acidic or basic dissolutions, named fluxing, solubilizing the protective oxide layer and then severely damaging the material integrity [11].

Despite its long period of use, little work has been carried out on the corrosion behavior of DS200 + Hf, studies focusing mainly on its overall mechanical behavior [18]. The aim of this paper is thus to evaluate the Type-II hot corrosion resistance of the DS200 + Hf nickel-based superalloy at 650 °C taking in account the influence of the non-metallic inclusions (MC carbides), the  $\gamma + \gamma'$  eutectic pools, the grain size and grain orientation of the superalloy. The last two are related to the Bridgman-Stockbarger solidification process [1] used to manufacture the DS200 + Hf alloy. Due to the casting process, the thermal gradient implies significant coarsening of the grain microstructure along the turbine blades, as well as a more pronounced crystallographic texture by variant selection. Some grains may also present a misorientation from the perfect  $\langle 001 \rangle$  crystallographic orientation of up to 10° [18]. This alloy with its peculiar microstructure can indeed be considered as a model alloy allowing for investigation of oxidation, sulfation, or sulfidation phenomena occurring at grain boundaries and the resulting degradation kinetics with very different microstructural patterns, i.e., grain boundaries, MC carbide and eutectics distributions, according to the sampling plane.

## Experimental Procedures

The nominal composition of the DS200 + Hf nickel-based superalloy is given in Table 1 [18]. Cast plates were supplied by Safran Aircraft Engines Gennevilliers (L x W x H: 110 × 65 × 15 mm<sup>3</sup>). All received a solution treatment: 1210 °C / 30 min, 1225 °C / 30 min and 1240 °C / 4 h with cooling above 45 °C/min to 700 °C followed

**Table 1** DS200 + Hf nominal composition (wt. %)

Element	Ni	Cr	W	Co	Al	Hf	Nb	Ti	C	B	Zr	Fe
Wt%	Bal	8.6	11.8	9.5	4.90	1.58	0.86	1.87	0.13	0.015	0.01	0.02

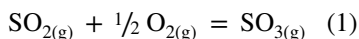
by quenching in air. Two tempering treatments at 1100 °C / 5 h and 870 °C / 16 h were then carried out, with air quenching after each heat treatment. Samples (L x W x H: 1.2 × 1.0 × 0.2 cm<sup>3</sup>) were cut by electrical discharge machining (EDM) and then ground to a P2400 surface finish with a precision JIG, enabling precise dimensional measurement of thickness as well as a limited and homogeneously distributed work hardening [19]. Each sample was cleaned with acetone then ethanol in an ultrasonic bath for 10 min. Four different sample configurations were tested: longitudinal fine grain (FGT), longitudinal coarse grain (CGL), transverse fine grain (FGT) and transverse coarse grain (CGT). Longitudinal (L) and transverse (T) samples are parallel and perpendicular to the growth direction of columns <001>, respectively. Grain size depends on the selection of the sample extraction location, taking into account granular coarsening due to the elaboration process. Fine-grain samples were taken from the bottom of the cast plates and coarse-grain samples from the upper region. Table 2 summarizes the different sample extraction location, orientations and average grain sizes.

Before corrosion testing, samples were pre-oxidized for 2 h at 700 °C to facilitate adhesion of the Na<sub>2</sub>SO<sub>4</sub> deposit, resulting in the formation of a 10-nm-thick oxide layer. An amount of 1 ± 0.1 mg/cm<sup>2</sup> Na<sub>2</sub>SO<sub>4</sub> was deposited on each side of the samples by spraying a saturated Na<sub>2</sub>SO<sub>4</sub> solution, the samples being pre-heated at 250 ± 20 °C on a hot plate prior to spraying. The homogeneity in terms of thickness of deposit was ensured using an argon-pulsed airbrush. (Measured thickness was less than 10 μm.) Corrosion tests were conducted in a tubular furnace fitted with a concentric quartz tube [See [9] for more details].

Samples were placed vertically in an alumina holder, at 650 °C. The gaseous atmospheres were obtained by diluting a mixture of synthetic air (20% O<sub>2</sub>, 80% N<sub>2</sub>) + 1%vol. SO<sub>2</sub> in synthetic air (20% O<sub>2</sub>, 80% N<sub>2</sub>). Type-II corrosion tests were performed isothermally in three different gases (air, air + 150 ppm SO<sub>2</sub>, air + 400 ppm SO<sub>2</sub>). The total flow rate was set to 80 ml/min and the heating rate at 10 °C/min. SO<sub>2</sub> was introduced in the flowing gas once the temperature of the furnace reached the isothermal setpoint. In air and at high temperature, sulfur dioxide SO<sub>2</sub> oxidizes to sulfur trioxide SO<sub>3</sub> according to Eq. (1).

**Table 2** Sampling plan for hot corrosion tests

Sample ID	FGT	FGL	CGT	CGL
Sampling area	Fine grains	Fine grains	Coarse grains	Coarse grains
Grain size range	160 – 350 μm	250 – 600 μm	0.5 – 1.7 mm	1.5 – 2.0 mm
Orientation	Transverse ⊥ <001>	Longitudinal/ /<001>	Transverse ⊥ <001>	Longitudinal/ /<001>



It is well known that  $\text{SO}_3$  formation, which is fundamental for the stabilization of  $\text{Na}_2\text{SO}_4 - \text{NiSO}_4$  and  $\text{Na}_2\text{SO}_4 - \text{CoSO}_4$  molten sulfate mixtures, is temperature-dependent [16, 17] and has to be catalyzed to reach equilibrium conditions. Nevertheless, Malacarne et al. [20] showed, using the same experimental setup, that the  $\text{SO}_2/\text{SO}_3$  contents in the outlet gas were close (difference of 2%) to the conversion rate theoretically expected from reaction (1). This one is 69%mol.  $\text{SO}_3$  and 31%mol.  $\text{SO}_2$  at equilibrium at 650 °C. Furthermore, the results presented hereafter demonstrate that reaction (1) occurs.

Weight gains were recorded for 24 h, 50 h and 100 h (all tests being strictly isothermal), with the 4 sampling configurations (FGT, FGL, CGT, CGL). Some tests were carried out at intermediate times (5 h and 36 h) when mass gain differences between two isothermal stages were judged too high. Mass was determined on a Mettler Toledo XS205 balance with a 0.01 mg precision. Post-exposure, samples were characterized by X-ray diffraction (Bruker D8 Advance) and then by scanning electron microscopy (FEG-SEM Thermo Fisher Scientific). Given the high solubility of sulfates in aqueous media, all preparations were performed using an ion polisher (JEOL CP6500). ImageJ2 (Fiji) software [21] was used for image analysis and quantification of corrosion depths.

## Results

### Initial Microstructure

The microstructure of DS200+Hf in the heat-treated condition at different scales is shown in Fig. 1. Chemical segregations are still present after solution heat treatment, as depicted in Fig. 1a. Dendritic and interdendritic solidification structure was clearly observed. Intra- and intergranular MC carbides, located in interdendritic regions, outlined the main  $\langle 001 \rangle$  orientation. The  $\gamma + \gamma'$  eutectic pools (darker area

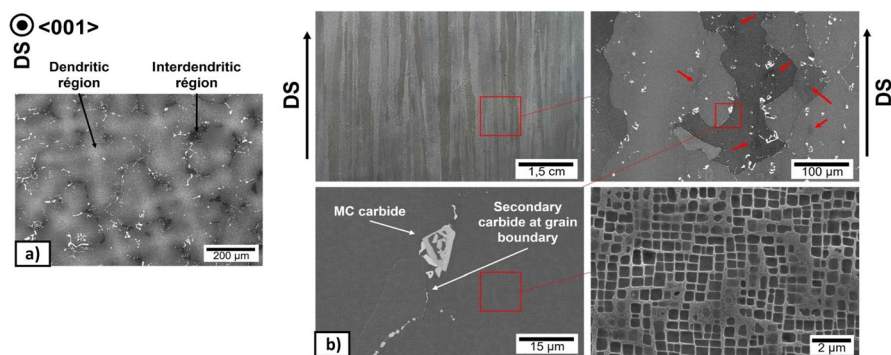


**Fig. 1** DS200+Hf—**a** Dendritic and interdendritic solidification structure; **b** Microstructure at various observation scales

in Fig. 1a and zones labeled with red arrows in Fig. 1b) were located in the interdendritic regions. Secondary carbides were localized at grain boundaries. The strong BSE contrast of MC carbides suggested local chemical variations in Hf, Nb, Ti and W elements. The  $\gamma + \gamma'$  eutectic pools constituted areas that were enriched with Ti, Al and depleted with Cr, Co and W. Ta and Zr elements were present in trace amounts in the MC carbides. High magnification observation (Fig. 1b) evidenced the typical cuboidal microstructure expected for these  $\gamma/\gamma'$  nickel-based superalloys. The edges of the cuboid were around 400 nm long.

### Corrosion Behavior of DS200 + Hf at 650 °C

Figure 2 shows the mass gains *vs* time at 650 °C of all DS200+Hf samples after testing (2.a) and the average of these values *versus* time (2.b), *i.e.*, independently of the sampling orientation, for a given gas mixture (air, air+150 ppm SO<sub>2</sub>, air+400 ppm SO<sub>2</sub>). Interestingly, grain orientation and grain size had no clear influence on the DS200+Hf Type-II corrosion rate. Mass gains were homogeneous and relatively reproducible from one test to another and from one grain size to another. Although fine-grain samples (transverse and longitudinal) showed higher mass gains in air+400 ppm SO<sub>2</sub> at 50 h and 100 h, the opposite trend was observed in air+150 ppm SO<sub>2</sub>. Mass variations tend to become increasingly significant with the duration of the exposure.

Conversely, the results were clearly correlated with the nature of the gaseous atmosphere. Samples exposed in air showed homogeneous mass gains with no significant evolution with time. For 100 h of testing, DS200 + Hf presented an average mass variation of  $0.21 \pm 0.03$  mg/cm<sup>2</sup>. The tests performed in air+150 ppm SO<sub>2</sub> experienced a similar behavior for the former 24 h. Then, an acceleration was noticed. Validation experiments carried out for 36 h confirmed this tendency. After 100 h of testing in this gas, samples gained in average  $2.92 \pm 0.30$  mg/cm<sup>2</sup> and showed significant spallation after mass measurements. For the tests in air+400 ppm SO<sub>2</sub>, rapid mass gains were observed from the very first moment. Again, spallation

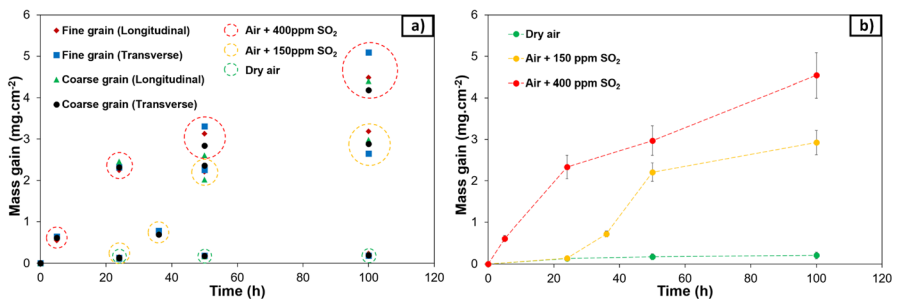


Fig. 2 DS200+Hf, coated with 1 mg/cm<sup>2</sup> Na<sub>2</sub>SO<sub>4</sub> in dry air, air+150 ppm SO<sub>2</sub> and air+400 ppm SO<sub>2</sub> at 650 °C **a** Mass gain *vs* time according to various sampling orientation (FGT, CGT, FGL, CGL); **b** Average of the values given in a) *versus* time, *i.e.*, independently of the orientation, for a given gas mixture

phenomena were sometimes observed after 100 h isothermal exposure. An average mass gain of  $4.54 \pm 0.40 \text{ mg/cm}^2$  was recorded after 100 h exposure.

Figure 3 shows representative cross sections of fine-grain transverse (FGT) samples exposed 50 h in the two  $\text{SO}_2$  containing atmospheres. It highlights the duplex morphology of the corrosion products, consisting of an outer homogeneous layer and an internal layer. It shows also a systematically greater depth of attack when MC carbides and  $\gamma + \gamma'$  eutectic pools are present at the surface or in the subsurface area, *i.e.*, for the interdendritic regions. In the end, the proportion of grain boundaries seems to have a lower impact on the corrosion rate than the proportion of MC and  $\gamma + \gamma'$  pools in the surface and subsurface zones.

These observations are combined in Fig. 4 using box plots for a statistical approach, quantifying the depth affected by corrosion by distinguishing dendritic and interdendritic regions. For all conditions, the difference between the interdendritic and dendritic regions increases with exposure time. In air, the affected depths were less than 5  $\mu\text{m}$ .

The strongest difference between interdendritic and dendritic regions in terms of depth of attack was observed at 150 ppm  $\text{SO}_2$ , with significant local pitting. After 100 h, the maximum affected depth was 23.0  $\mu\text{m}$  in the interdendritic region and only 9.0  $\mu\text{m}$  for the dendritic one. This behavior was less pronounced in air+400 ppm  $\text{SO}_2$ , but the overall corrosion rate was higher. Thus, a slightly more homogeneous degradation was observed between both regions.

As shown in Fig. 2b, the most severe conditions corresponded to air+400 ppm  $\text{SO}_2$ . The alloys presented the highest depth of attack, with a maximum of 45.5  $\mu\text{m}$  after 100 h of exposure. Relative deviation determined from medians showed differences in the affected depths between interdendritic and dendritic area of 34.0% in air, 49.5% in air+150 ppm  $\text{SO}_2$  and 30.7% in air+400 ppm  $\text{SO}_2$ .

Figure 5 shows the cross sections of the fine-grain samples in the longitudinal direction (FGL) at 24, 50 and 100 h for the three gas mixtures. In the case of dry air tests, a compact layer of mainly sodium sulfate formed on the alloy surface. A few corrosion products developed externally *vs* time; they consisted of nickel and cobalt

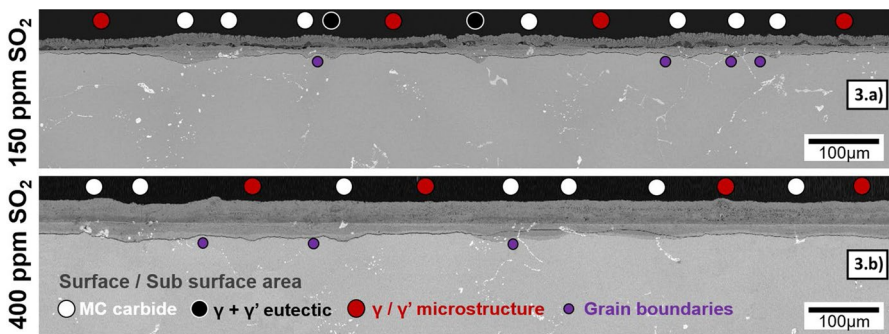


Fig.3 Surface degradation of DS200+Hf (FGT) at 650 °C 50 h in **a** air+150 ppm  $\text{SO}_2$  and **b** air+400 ppm  $\text{SO}_2$ . White disks are for MC carbides-rich region; red for  $\gamma/\gamma'$  microstructure; and black for  $\gamma + \gamma'$  eutectic pools and purple for grain boundaries

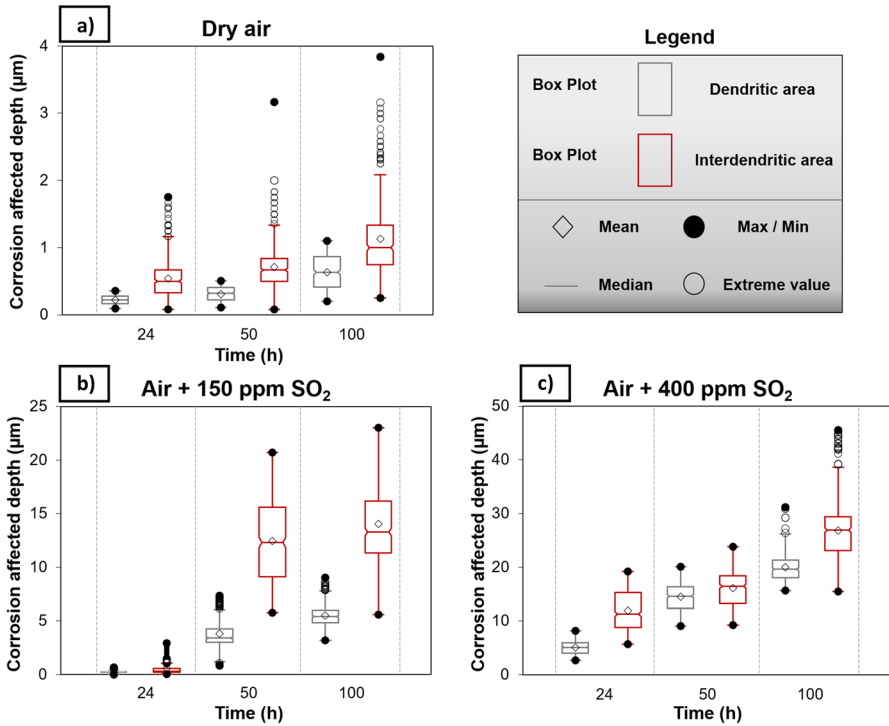


Fig.4 Box plot representing the depth of attack for dendritic and interdendritic locations (where MC carbides MC and  $\gamma+\gamma'$  eutectic pools are present) at 650 °C for 24 h, 50 h, 100 h in a dry air, b air + 150 ppm SO<sub>2</sub> and c air + 400 ppm SO<sub>2</sub>

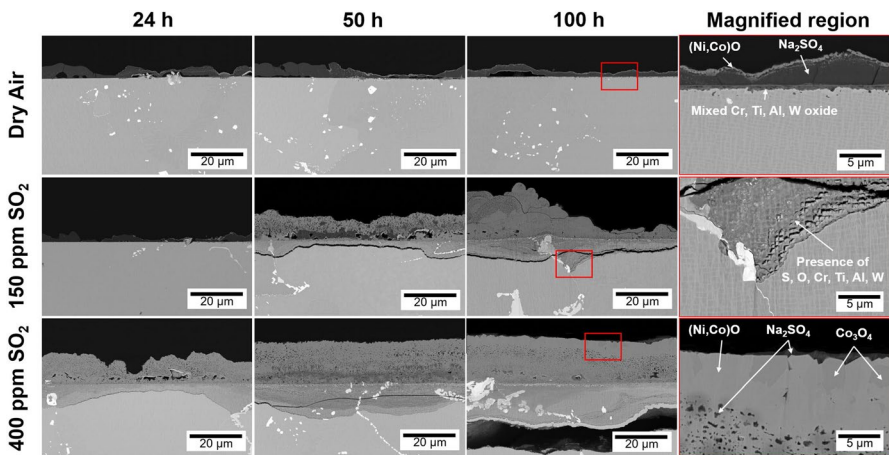


Fig.5 DS200+Hf (FGL) with  $\langle 001 \rangle$  axis perpendicular to the observation) coated with 1 mg/cm<sup>2</sup> Na<sub>2</sub>SO<sub>4</sub> at 650 °C; Microstructural evolution vs time in dry air, air + 150 ppm SO<sub>2</sub> and air + 400 ppm SO<sub>2</sub>

oxides. Chromium, aluminum, titanium and tungsten formed oxides internally. The initial interface of the sample remained clear. EDS measurements were performed in the sodium sulfate layer. The results revealed the presence of a low amount of nickel (1.1; 6.9; 7.6%wt.) and cobalt (0.0; 3.7; 5.4%wt.) for the 24, 50, 100 h test durations, respectively.

For air + SO<sub>2</sub>, the formation of the duplex outer and internal layers was systematically observed. Their thickness was growing with time of exposure. The MC carbides appeared to be fully embedded in the internal oxide layer. The morphology of the carbides inside the internal oxide layer evidenced that they did not undergo diffusion process to a large extent.

For 150 ppm SO<sub>2</sub>—24 h of exposure, the cross section was similar to that observed in air. At 50 h, further degradation was observed with severe attack in the location of MC carbides and  $\gamma + \gamma'$  eutectic pools. The sulfate residues observed for this SO<sub>2</sub> containing atmosphere showed lamellar structures with significant nickel enrichment (5 to 34%wt) and cobalt (5 – 17%wt). The Ni and Co content of the sulfate mixture was, however, difficult to interpret in view of the surrounding oxide layers also captured during EDX measurements and contributing to the results. The development of the outer (Ni, Co)O layer was enhanced, trapping Na<sub>2</sub>SO<sub>4</sub> residues. The NiO phase was Co-enriched; a positive gradient of Co was noticed in this (Ni,Co)O layer up to the oxide/atmosphere interface. The internal corrosion products mainly consist of S, O, Al, Cr, Ti and W. The chemistry and morphology of this fine mixture of oxide, of sulfate and sulfur forming internally, will be features to consider for further studies.

In air + 400 ppm SO<sub>2</sub>, the corrosion attacks were quite similar to the ones observed for air + 150 ppm SO<sub>2</sub>, but noticeably accelerated. The SO<sub>x</sub>-rich atmosphere clearly favored faster reaction rate. This progress was materialized by a significant formation of a homogeneous outer layer of 25- $\mu$ m-thick (Ni, Co)O, with increased partitioning of Co; Co<sub>3</sub>O<sub>4</sub> grains forming in the outer layer. Sodium sulfate appears to be incorporated during the development of the outer layer. Intragranular and intergranular MC carbides combining with  $\gamma + \gamma'$  eutectic pools were again preferential pitting zones compared to the  $\gamma/\gamma'$  microstructure. In the  $\gamma/\gamma'$  area, the corrosion products morphology clearly evidenced the characteristic cuboidal microstructure of the heat-treated superalloy.

## Discussion

The present study was performed at 650 °C to identify the morphology of the Type-II hot corrosion attacks for the DS200 + Hf nickel-based superalloy. The relationship between hot corrosion rate and microstructural components was considered at different scales and for three environments allowing to cover a wide range of SO<sub>2</sub> amount. All experiments were performed using  $1 \pm 0.1$  mg.cm<sup>2</sup> sodium sulfate deposit. Experimental results and analyses were carried out on a total of forty-five samples, including different sampling strategies, test conditions (air, air + 150 ppm SO<sub>2</sub> and air + 400 ppm SO<sub>2</sub>) and exposure times (24, 50 and 100 h). The results are discussed

hereafter focusing on the role of grain size and sample orientation, the contribution of the different microstructural features and the effect of  $\text{SO}_2$  on the corrosion rate.

### **Effect of Grain Size, Sample Orientation and Microstructure**

The influence of grain size was studied with samples taken from the fine- and coarse-grain regions of the directionally solidified ingot. Transversal and longitudinal orientations were selected in both regions. Despite a higher grain boundary density for fine-grain samples than for coarse-grain samples, the change in mass (Fig. 2) was not significantly affected whether the sample was taken in the transverse or longitudinal direction.

This finding indicates that the grain size and grain orientation are not first order parameters for the degradation of DS200 + Hf superalloys. At 650 °C, diffusion phenomena both in the bulk of the alloy and at alloy grain boundaries were slow. Therefore, degradation was not affected by grain size.

Surprisingly, this macroscopic observation (Fig. 3) was accompanied by highly selective degradation and deeper attacks, systematically observed when MC carbides and  $\gamma + \gamma'$  eutectic pools were present at the surface and in the subsurface region. This was statistically demonstrated (Fig. 4) on a population of over 500 measurements for each test condition and exposure time. As the MC carbides and  $\gamma + \gamma'$  eutectic pools were mainly located in the interdendritic regions (Fig. 1a), the difference of depth of attack was mainly a result of the solidification process.

The DS200 + Hf microstructure kept in fact residual characteristics of the solidification stage despite the high temperature solution treatment (4 h—1240 °C). The difference of depth of attack between dendritic and interdendritic regions was more pronounced in air and air + 150 ppm  $\text{SO}_2$  than in air + 400 pm  $\text{SO}_2$  because of the higher corrosion rate observed for the latter environment.

The results obtained on the influence of  $\gamma + \gamma'$  eutectic pools on affected depths are in good agreement with the observations of Chapman et al.[22] made on the directionally solidified CM274LC DS grade at 550 °C, but contrary to those mentioned by Lortrakul et al.[10] for CMSX-4 at 700 °C. DS200 + Hf / CM427LC DS grades have a close composition, as well as the same local element segregation between dendritic/interdendritic regions. This can explain the similar behavior observed for both alloys. The  $\gamma + \gamma'$  eutectic pools for DS200 + Hf and CM427LC DC are characterized by a higher volume fraction of  $\gamma'$  due to coarsening phenomenon and chemical depletion (Cr, Co, W) regardless the  $\gamma/\gamma'$  zones.

The present results traduced the poor resistance of the  $\gamma'$  phase as reported by Mathieu et al. [23]. for the TROPEA single crystal nickel-based superalloy. The authors evidenced that the  $\gamma'$  oxidation mainly formed unprotective NiO in air in this range of temperature, whereas the  $\gamma$  phase developed protective  $\text{Cr}_2\text{O}_3$  or  $\text{NiCr}_2\text{O}_4$ . The decrease in chromium and cobalt in the eutectic pools further partitions nickel in these areas fostering the formation of unprotective oxide scale. Thus, the higher volume fraction of  $\gamma'$  in the eutectic pools is prejudicial to the corrosion resistance of the DS200 + Hf. Considering MC carbides, Suave et al. [18] reported their poor intrinsic oxidation resistance associated with the rapid formation of  $\text{HfO}_2$ .

They evidenced that once MC carbides are oxidized, a significant amount of NiO formed in their neighborhood. This was due to the fact that primary carbides and eutectic pools were related to the same segregation phenomenon happening during the solidification stage. Thus, strong difference of corrosion behavior was observed between dendritic and interdendritic regions.

### **Influence of the SO<sub>2</sub>/SO<sub>3</sub> Amount**

Firstly, it is assumed that the air + SO<sub>2</sub> inlet gas evolves in the presence of catalytic surfaces toward a SO<sub>2</sub>/SO<sub>3</sub> mixture, associated with a supposed composition ratio of 69% SO<sub>3</sub> and 31% SO<sub>2</sub> at equilibrium, according to Malacarne et al. at 650 °C [9].

Figures 2, 4 and 5 clearly show that the higher the SO<sub>2</sub> concentration in the gaseous environment, the more severe the degradation of the samples, regardless of the sampling conditions. The difference of mass was observed as early as 5 h of testing when comparison was made between air + 150 ppm SO<sub>2</sub> and air + 400 ppm SO<sub>2</sub>. If the occurrence of an incubation period before the propagation can be proposed for the test with 150 ppm SO<sub>2</sub>, the propagation started immediately for air + 400 ppm SO<sub>2</sub>. Thus, the incubation period was shortened, and the corrosion rate was higher with an increase in SO<sub>2</sub>/SO<sub>3</sub> content.

It is widely accepted that the incubation period corresponds to the required time for the formation of a molten salt. In the present case, the liquid formation should result from the sulfation of NiO and CoO oxides [24] and then their solubilization with Na<sub>2</sub>SO<sub>4</sub>, forming a Na<sub>2</sub>SO<sub>4</sub> – (Ni/Co)SO<sub>4</sub> solid solution mixture. The higher the amount of SO<sub>3</sub> in the gaseous environment, the more quantitative the sulfation occurs [24]. The mixture will subsequently reach the solidus composition more rapidly and will begin to melt. Once the first drop of liquid has formed, the reactions of dissolution (fluxing) of the protective oxides can start. The alloy is hence not protected anymore. It seems clear that the higher the amount of NiO or CoO, the more likely the formation of liquid is, especially in the area of primary carbides and eutectic pools, as saw previously.

Higher corrosion rate with an increase in SO<sub>2</sub>/SO<sub>3</sub> content was previously observed by Kistler et al. [8] for the PWA1484 nickel-based single crystal superalloy for SO<sub>2</sub> composition ranging from 2.5 ppm to 100 ppm, but in a temperature domain in which the formation of a molten phase was not expected. Thus, the results evidenced that the sulfur-bearing species also controlled the reaction rate. The absence of a protective oxide layer at the DS200 + Hf interface does not support the hypothesis of a fluxing mechanism to explain the propagation stage. On the contrary, the observations corroborate the SO<sub>3</sub>-induced hot corrosion mechanism and the SO<sub>3</sub> oxidizing character [9].

Interestingly, the corrosion morphologies of DS200 + Hf in Fig. 5 showed that corrosion propagates along two distinct fronts. The region in the vicinity with the alloy was enriched in S and O, whereas the second was enriched in O. This was also supported on several  $\gamma/\gamma'$  grades (CMSX-4 [10, 22, 25], CM427LC DS [22], René N5 [25], LDS1101 [25], CMSX-10N [26]). Further characterizations are in progress

to better understand the nature of these layers and corrosion mechanisms at both dendritic and the  $\gamma/\gamma'$  scale of these  $\gamma/\gamma'$  nickel-based superalloys.

## Conclusions

The investigation of Type-II hot corrosion behavior of the DS200 + Hf nickel-based superalloy at 650 °C has established that i) the amount of SO<sub>2</sub> in the inlet gas is the main factor of degradation, undoubtedly affecting both the duration of the initiation stage and the corrosion rate; ii) the proportion of grain boundaries and their orientation have no influence on degradation kinetics; and iii) MC carbides and  $\gamma + \gamma'$  eutectic pools, *i.e.*, interdendritic regions, are detrimental for Type-II hot corrosion, with deeper attacks observed regardless of the gaseous atmosphere. The global mechanism can be explained by the SO<sub>3</sub>-induced hot corrosion mechanism. Although the composition of the outer layers has been identified as (Ni,Co)O solid solution, the nature of the intricated phases in the inner zone remains to be determined.

**Acknowledgements** The Safran group is gratefully acknowledged for its financial support, technical meetings and G. Dufour PhD thesis grant. Jonathan Cormier (Institut Pprime) is gratefully acknowledged for providing the materials.

**Author Contribution** G.D contributed to methodology, formal analysis, writing—original draft, and review and editing. S.M was involved in conceptualization, validation, supervision and review and editing. D.T contributed to conceptualization, validation, supervision and review and editing. T.S was involved in resources, validation and review and editing. T.P contributed to resources, validation and review and editing. J.B was involved in resources, validation and review and editing. S.K contributed to resources, validation and review and editing. D.B was involved in investigation. M.V contributed to validation, supervision and review and editing.

**Data Availability** No datasets were generated or analyzed during the current study.

## Declarations

**Conflict of interest** The authors declare no competing interests.

## References

1. A. Baldan, *Journal of Materials Science* **26**, 1991 (3879).
2. D. N. Duhl and C. P. Sullivan, *Journal of Metals*. **7**, 1971 (38).
3. Z. Yunrong, W. Yuping, X. Jizhou, et al., *The Metallurgical Society Superalloys* **1988**, 1988 (335).
4. R. Sellamuthu and A. F. Giamei, *Metallurgical Transactions A* **17**, 1986 (419–428).
5. H. E. Collins, *American Society Metals* **62**, 1969 (82).
6. G. Lvov, V. I. Levit, and M. J. Kaufman, *Metallurgical and Materials Transaction A* **35A**, 2004 (1669–1679).
7. F. Pettit, *Oxid of Metals* **76**, 2011 (1).
8. E. Kistler, W. T. Chen, G. H. Meier, et al., *Materials and Corrosion*. **1**, 2019 (1346).
9. R. Malacarne, S. Mathieu, L. Aranda, et al., *Corrosion Science* **224**, 2023 (111550).
10. P. Lortrakul, R. W. Trice, K. P. Trumble, et al., *Corrosion Science*. **80**, 2014 (408).
11. R. A. Rapp, *Corrosion Science*. **44**, 2002 (209).
12. K. P. Lillerud, Kofstad P. *Oxidation of Metals* **21**, 1984 (233–270).
13. Giggins C.S, Pettit F.S, Hot Corrosion Degradation of Metals and Alloys A Unified Theory, (1979).

- 14 J. A. Goebel, F. S. Pettit, and G. W. Goward, *Metallurgical Transactions*. **4**, 1973 (261).
15. Young D.J., (2016). *High Temperature Oxidation and Corrosion of Metals (Second Edition)*. 603
16. Misra A.K, Whittle D.P, Worrell W.L., *J. Electrochem. Society : solide-state science and technology* (1982).
- 17 K. L. Luthra and D. A. Shores, *Journal of The Electrochemical Society* **127**, 1980 (2210).
18. L. M. Suave, J. Cormier, et al., *The Minerals, Metals and Materials Society Superalloys* **2018**, 2016 (747).
- 19 D. Texier, D. Monceau, et al., *Materials at High Temperatures* **33**, 2016 (325).
20. Malacarne R, 2021. *Etude de l'oxydation et de la corrosion à haute température d'alliages base nickel polycristallins*, PhD Thesis, Lorraine University.
- 21 C. T. Rueden, J. Schindelin, Hiner, et al., *BMC Bioinformatics*. **18**, 2017 (1).
- 22 N. Chapman, S. Gray, J. Summer, and J. Nicholls, *Oxidation of Metals*. **97**, 2022 (261).
23. Mathieu S, Podor R, Emo M et al., *High Temperature Corrosion of Materials* ; under review (2024).
- 24 R. Malacarne, S. Mathieu, et al., *Corrosion Science*. **218**, 2023 (111186).
25. J. L. Smialek and S. Gray, *Materials* **11**, 2018 (2098).
26. Y. Koizumi, K. Kawagishi, et al., *The Minerals, Metals and Materials Society Superalloys* **2020**, 2020 (747–752).

## Authors and Affiliations

**G. Dufour<sup>1,2,3</sup> · D. Texier<sup>2</sup> · T. Sanviemvongsak<sup>3</sup> · T. Perez<sup>3</sup> · J. Bonnal<sup>4</sup> · S. Knittel<sup>4</sup> · D. Bonina<sup>1</sup> · M. Vilasi<sup>1</sup> · S. Mathieu<sup>1</sup>**

- ✉ G. Dufour  
gregoire.dufour@safrangroup.com
- D. Texier  
damien.texier@mines-albi.fr
- T. Sanviemvongsak  
tom.sanviemvongsak@safrangroup.com
- T. Perez  
thomas.perez@safrangroup.com
- J. Bonnal  
justine.bonnal@safrangroup.com
- S. Knittel  
stephane.knittel@safrangroup.com
- D. Bonina  
david.bonina@univ-lorraine.fr
- M. Vilasi  
michel.vilasi@univ-lorraine.fr
- S. Mathieu  
stephane.mathieu@univ-lorraine.fr

- <sup>1</sup> Université de Lorraine, CNRS, Institut Jean Lamour, Campus Artem, 54011 Nancy, France
- <sup>2</sup> Institut Clément Ader (ICA) - UMR CNRS 5312, Université de Toulouse, CNRS, INSA, UPS, Mines Albi, ISAE-SUPAERO, Campus Jarlard, 81013 Albi Cedex 09, France
- <sup>3</sup> SafranTech, Rue des Jeunes Bois, 78117 Châteaufort, France
- <sup>4</sup> Safran Aircraft Engines, Rue Henri Auguste Desbruères, 91000 Evry, France